Stress Dependency of Permeability and Porosity Using Micromechanics Digital Rock

Guangyuan Sun*, *Zhuang* Sun, *Rafael* Salazar-Tio, *Andrew* Fager, *Bernd* Crouse

Dassault Systèmes, USA

Abstract. Understanding the impact of stress on porosity and permeability properties of rocks is crucial to study the fluid flow in subsurface formation rocks. The micro-pore structure of subsurface reservoirs can change when the reservoir stress field is disrupted. In this paper, we present a digital rock workflow to couple micromechanics model with Lattice Boltzmann fluid model. Micromechanics models uses a robust grain-grain segmentation method, a conformal meshing algorithm, and the grain-grain contact physics. The porosity and permeability variations are measured under different conditions of stress magnitudes. The results of permeability measurements indicate that tighter core samples are more stress dependent. The average diameter and distribution of pore size have also been calculated in order to investigate the effect of stress on average pore diameter. The effective permeability simulated by the multiphase digital rock model is compared to demonstrate the influence of stress on the flow behaviors.

1 Introduction

The understanding of the stress-sensitive behavior of rock porosity and permeability play a significant role to study the fluid flow in subsurface formations. The micro-pore arrangement within subsurface reservoirs may undergo alterations when the stress field of the reservoir is changed due to the drilling and subsequent operations. Consequently, the porosity, permeability, and other significant physical characteristics of the reservoir can undergo modifications accordingly.

Numerous laboratory experiments have explored the stress-dependent behavior of porosity and permeability in rock and fault gouges, which are unconsolidated rocks characterized by small grain size. In all the experiments, it has been observed that the effective stress plays the most significant role in modifying the magnitude of porosity and permeability. The trend of permeability and porosity under varying stress conditions can be described using two types of models: power law and exponential equations.

For the power law form of equation, a general relation between stress and permeability or porosity of rocks is written as,

$$Y = Y_0 \left(\frac{\sigma_e}{\sigma_0}\right)^{-n} \tag{1}$$

where Y is porosity (in fraction) or permeability (in mD) under effective stress σ_e (in psi), Y_0 is initial porosity (in fraction) or permeability (in mD) at σ_0 (in psi) and n is material constant. It is noted that the values of material constant control the rate of stress dependency of rock properties. The equation above has been extensively used by researchers. Shi and Wang [1] proposed that a power law form could effectively describe the relationship between effective stress and permeability of fault gouges based on the permeability values [2]. They found that the material constant parameter varies between 1.2 and 1.8. Another study [3] on the stress dependency of sandstone and shale core samples from TCDP Hole-A shows material constant be in the range of 0.120-1.744 for the permeability and 0.014-0.056 for the porosity.

Exponential or logarithmic relationships between stress and rock properties have also been applied. The exponential or logarithmic equation that establishes the connection between stress and either porosity or permeability is described as,

$$Y = Y_0 \exp\left(-n(\sigma_e - \sigma_0)\right) \tag{2}$$

or

$$Ln\frac{Y}{Y_0} = -n(\sigma_e - \sigma_0) \tag{3}$$

Many studies have used the above exponential (or logarithmic) form of equation for various kinds of samples. David et al. [4] reported exponential correlation for different types of sandstones. The materials constants for the permeability and porosity parameters were in the range of 0.00621–0.0181 MPa^{-1} and 0.00044–0.0033 MPa^{-1}, respectively. Teklu et al. [5] studied the stress dependency of porosity and permeability of carbonate, limestone, and sandstone core samples described by the above exponential form. They observed that the stress dependency of permeability and porosity is larger for nanodarcy cores compared with those of micordarcy and millidarcy core samples. Similarly, the stress dependency of porosity has been observed by many researchers. Schmoker et al. [6] suggested an exponential relation between effective stress and porosity for carbonate rocks. Hoholick et al. [7] found an exponential equation form of porosity-stress dependency for sandstone rocks. An empirical logarithmic model proposed by Jones and Owens [8] and theoretically derived by Walsh [9] is selected to evaluate the stress sensitivity for the porosity and permeability of tight gas sands. The stress sensitivity is defined by the stress sensitivity coefficient S_s, which is described as,

$$S_s = \frac{1-(Y/Y_0)^{\frac{1}{3}}}{log(\sigma_e/\sigma_0)} \tag{4}$$

* Corresponding author: Guangyuan.SUN@3ds.com

It seems that most of the reported studies have been only focused on the conventional lab measurements. The challenges of the experiments are due to the fact that they are expensive and time-consuming and could lead to the damage of the core samples under the stresses applied. There are also studies reported on numerical simulations to understand the stress dependency of porosity and permeability magnitudes. Petunin et al. [10] found that a heterogeneous multi-porosity system is more stress-sensitive compared to the other more homogeneous porosity systems. Sun et al. [11, 12] showed that grain crushing occurring at a very high effective stress tends to produce fines and have a significant impact on the permeability based on the discrete element method. Fagbemi et al. [13] simulated the deformation of a sandstone rock using a finite element method and the fluid flow using a finite volume method andfound that the oil-phase relative permeability reduced due to the increase in stress loading. Fan et al. [14] investigated the single/multi-phase fluid flow in a proppant pack of hydraulic fracture and showed that the oil-phase relative permeability first increased but then decreased as the effective stress was continuously increased.

In the recent years, digital rock physics has been developed as a powerful technology to accurately predict fluid behavior in porous media. It involves the construction of 3D representation structures from pore-scale imaging and offers a direct presentation of multiphase flow properties at reservoir conditions. The technology combines 3D imaging technology such as X-ray micro-computed tomography (CT) with high performance computational modeling, and thus enables numerical measurements of flow behavior on large complex pore structures obtained from pore-scale image of a rock sample directly. Flow simulations based on the Lattice Boltzmann method (LBM) have proven successful due to the accuracy on capturing the relevant physics of single-phase and multiphase flow [15-18].

In the previous study [19, 20], we introduced a micro-CT based models and modeled the grain-grain contacts using grain-grain segmentation method and a conformal meshing algorithm. We are able to provide physics-based simulations of general non-linear contact interactions and compute rock elastic properties. In this study, we describe an extension of the micromechanics workflow above to digital rock permeability simulations to numerically investigate the impact of stress variations on the porosity and permeability changes.

2 Methodology

2.1 Micromechanics workflow

The micromechanics workflow combines a grain-grain segmentation method, a grain meshing algorithm, and a grain-grain contact physical simulation. A detailed description of the micromechanics workflow can be found in our previous publications [19, 20]. We review the methodology here for the purpose of completeness.

The grain-grain segmentation method assigns each grain voxel in the micro-CT image the value of the corresponding grain index and provides basis for subsequent mesh creation. We implement a variant of the watershed method to avoid the undesired features such as grouped grains and single grain cut. The grain meshing algorithm is based on Delaunay refinement combined with global and local optimizers to optimize the Delaunay triangulation. The algorithm will result in conformal meshing at the grain-grain contacts which enables the capture of contact physics. The meshing density was optimized to achieve a balance between accuracy and computational cost. The grain-grain contact physics simulation takes advantage of a non-linear finite element simulation based on Abaqus™/Explicit [21]. The grain-grain contacts introduce duplicate nodes and elements to allow grain relocation and relative displacement along contact surfaces. The normal contact behaviour follows a “hard” contact with penalty enforcement and the tangential contact behaviour adopts the classical Coulomb friction model. The general contact algorithm is used to detect contacts automatically for all element-based surfaces.

2.2 Lattice Boltzmann method

The lattice Boltzmann method (LBM) is a computational fluid dynamics (CFD) technique that has gained popularity among petroleum engineers for its suitability to simulate fluid flow in complex geometries such as in reservoir rock porous structures. It offers a unique and efficient approach to model complex multiphase flow phenomena, such as oil and gas reservoir behavior, with its ability to capture both macroscopic and mesoscopic flow properties. LBM is well-suited to simulate complex phenomena such as multicomponent fluid interaction, fluid-solid interaction, immiscibility, and capillary effects. All flow simulations were performed using DigitalROCK™, which uses a numerical solver based on the Shan-Chen multi-phase lattice Boltzmann model [22]. This solver has been validated on a variety of fundamental benchmarks and real reservoir rock test cases [15-18, 23-26].

2.3 Numerical simulation procedure

The samples were subjected to incremental displacements in all three directions with the normal degree of freedom controlled on the face nodes. We consider empty pores in the simulation (i.e. no pore pressure). Therefore, bulk modulus can be measured from the slope of the linear relationship between stress and volumetric strain. Each simulation takes around 4 hours of turnaround time on 40 computational cores. Abaqus™ can export STL surface mesh representing the deformed geometry at different time steps. We then convert the STL to voxel image for subsequent fluid flow simulation taking advantage of the stl-to-voxel python package (https://github.com/cpederkoff/stl-to-voxel).

In the next step, we perform the following for fluid flow simulations. (1) The resulting three-dimensional pore structures at various stress conditions are imported into LBM solver. (2) The single phase flow is simulated to measure absolute permeability. In the current study, each single phase simulation requires 300 simulation hours on 400 computational cores and the turnaround time is within one hour. (3) In the multiphase simulation, an unsteady-state displacement method is applied to measure relative permeability of water-oil displacement. 5% initial water saturation is chosen for multiphase simulations. All of the surfaces are assigned with 30º contact angle to establish the

uniform distribution of water-wet condition. The simulations of unsteady-state displacement requires 85,000 simulation hours on 1000 computational cores and the turnaround time is three to four days.

2.4 Rock sample

In this study, we work on sandstone samples. The binary segmented micro-CT image is available from the supplemental material of Andra et al. [27]. The original sample size is 288×288×300 and the image resolution is 7.5 μm. In order to investigate the effect of sample porosity, we create a second sample of high porosity by expanding the pore volume based on the Potts grow filter implemented in our in-house scripts. The porosity of two samples under initial condition are 12.67% and 23.82%, respectively. Figure 1 shows the binary and grain-segmented micro-CT images for these two sandstone samples.

In the simulation, the connectivity of the sample is determined by the minimum numerical critical pore throat.It is found that the numerical critical pore throat radius is 1.6 and 3.0 pixel. This indicates that the pore structure is barely connected due to insufficient numerical resolution. In order to achieve numerical accuracy of permeability measurement, the image resolution of low and high porosity samples is increased by a factor of 2 and 1.5, respectively. The absolute permeability measured by the single phase LBM solver under initial condition is listed in Table 1. Comparing the results for Fontinebleau with laboratory data [28] reveals that the simulation results are above those measured in the laboratory. The difference could be due to different critical pore throat radius measured in the current sample. Andra et al. [27] reported that their computed permeabilities on the same digital sample are generally larger than laboratory measurements. The sandstone sample of a small porosity has a bulk modulus of 7.2 GPa and the sandstone sample of a large porosity has a bulk modulus of 6.0 GPa, both of which are typical moduli for sandstones. Figure 2 shows the stress-volumetric strain relations where the bulk modulus is derived from the slope of the curve.

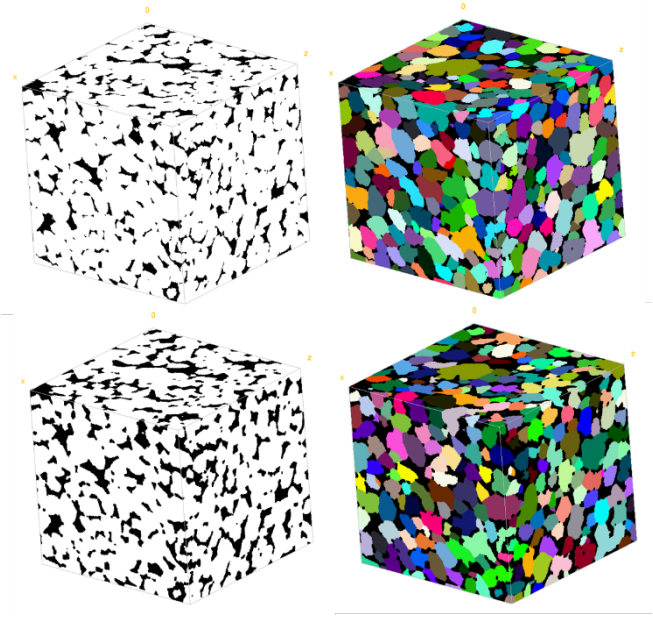

Fig. 1. Binary and grain-segmented images for (top) a sandstone sample of 12.67% porosity and (bottom) a sandstone sample of 23.82% porosity.

Table 1. Absolute permeability (K_0) under initial condition.

Initial porosity [%]	K_0 [mD] (X direction)	K_0 [mD] (Y direction)	K_0 [mD] (Z direction)
12.67	774	696	818
23.82	8912	8462	8982

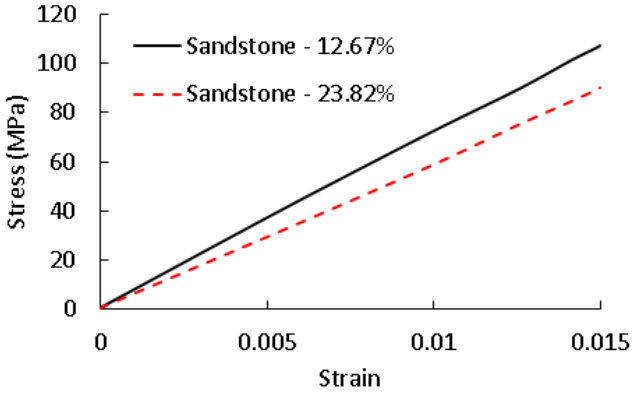

Fig. 2. Stress-strain relations for sandstones of a porosity of 12.67% and 23.82%, respectively.

3 Results and discussion

3.1 Stress-dependent porosity

The stress-porosity correlation is illustrated in Figure 3 and shows the evolution of the porosity variation for two tested samples. The porosity is normalized to show the variation. In principle, both the exponential effective stress correlation (Eq. 2 and 3) and the logarithmic correlation (Eq. 4) can be used to establish the relationship between effective stress and porosity, with the former being more straightforward. Linear regression analysis is applied to determine the material constant and corresponding parameter of determination (R^2) of porosity and permeability. The high value of R^2 indicates the simulation data fit well with Eq. 2 and 3, and the material constant obtained from the exponential correlation is reliable.

As listed in Table 2, the decrease in porosity is best described by an exponential relationship with increasing effective stress (R^2 = 0.9879-0.9999). This exponential material constants are 0.000199 and 0.000155 MPa^{-1} for tight sample and loose sample, respectively. David et al. [4] describe the similar range of the exponential material constants of stress-dependent porosity for sandstone samples. The higher value of material constant indicates a stronger reduction in porosity with increasing effective stress. The initial porosities of tight and loose samples are reduced by up to 2.1% and 1.6%, respectively. Thus, tight sandstone sample shows more sensitivity of porosity to effective stress and the materials constant is dependent on specific rock characteristics.

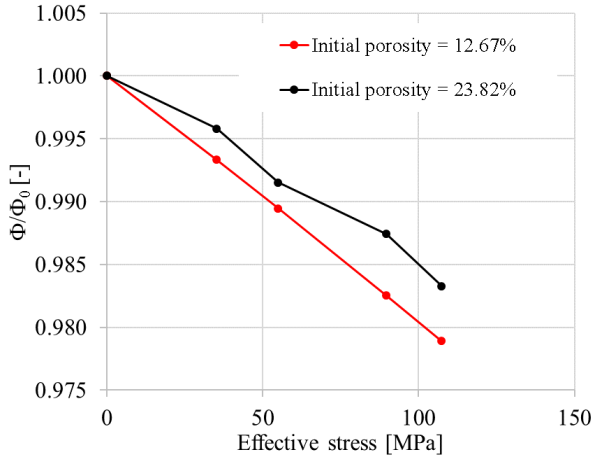

Fig. 3. Stress dependent porosity of the Fontainebleau core samples.

Table 2. Stress sensitivity (material constant) to porosity.

Initial porosity [%]	Material constant [10^{-4} MPa^{-1}]	R^2
12.67	1.99	0.9997
23.82	1.55	0.9879

3.2 Stress-dependent absolute permeability

To analyse the effect of effective stress on the permeability for different samples, the permeability values are normalized by dividing the resultant permeability at any effective stress to the initial permeability. As shown in Figure 4, when the effective stress increases, the permeability decreases. As with effective porosity, the stress-permeability relationship can best be described by the exponential equation with R^2 = 0.9604 - 0.9993 (Table 3). The material constant is determined for each sample and indicates a stronger stress dependence with higher material constant value. The stress-permeability correlation yields the material constant of 0.000748-0.000850 and 0.000606-0.000638 MPa^{-1} for tight and loose samples, respectively (Table 3). The results of permeability measurements indicates that tighter core samples are more stress dependent. This observation is consistent with David et al. [4] who reported that low porosity rocks have higher material constant and more stress-sensitive permeability. They demonstrated higher constant range for exponential relationship between effective stress and compaction-induced permeability. The difference on material constant range is mainly due to much less microfracture observed in the samples of this study.

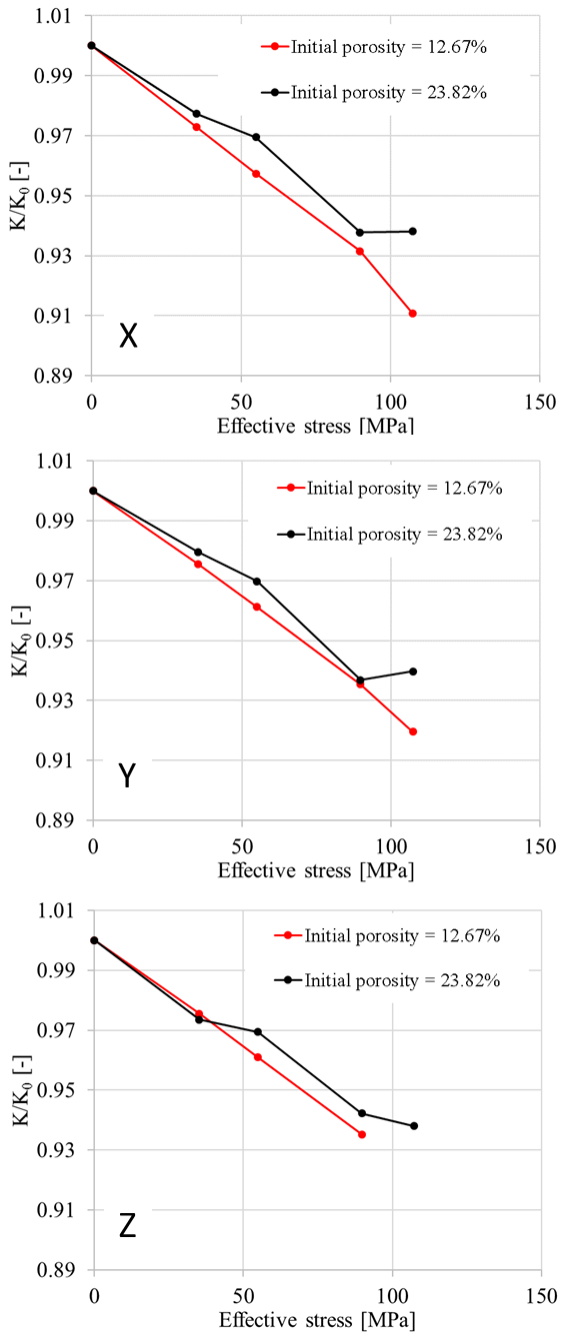

Fig. 4. Stress dependent permeability of the Fontainebleau core samples in X, Y, Z directions.

Table 3. Stress sensitivity (material constant) to permeability.

X Direction	Initial porosity [%]	Material constant [10^{-4} MPa^{-1}]	R^2
	12.67	8.50	0.9937
	23.82	6.38	0.9718
Y Direction	**Initial porosity [%]**	**Material constant [10^{-4} MPa^{-1}]**	**R^2**

	12.67	7.77	0.9973
	23.82	6.38	0.9604
Z Direction	**Initial porosity [%]**	**Material constant [10^{-4} MPa^{-1}]**	R^2
	12.67	7.48	0.9993
	23.82	6.06	0.9811

Figure 5 shows a unimodal distribution of pore size for the samples with initial averaging pore diameter of 47.10 µm and 53.63 µm for tight and loose samples, respectively (Table 4). As the sample being compressed, the distribution of pore volume shifts to the right indicating pore shrinking and throat necking. The pore size is reduced by 1.27% - 1.42%. Figure 4 demonstrates multi-directional analysis to evaluate anisotropy. In general, both of the samples show consistent stress-permeability paths in all three directions due to the homogeneous pore distribution of sandstone samples. When initial porosity = 12.67%, the relative variation in permeability shows the similar reduction up to 9.0% at maximum effective stress. When initial porosity is higher at 23.82%, the sample shows less sensitivity to stress and the permeability reduces by 6.1% at maximum effective stress.

For permeability, the dependency on initial pore volume is of secondary importance since the development of the pore geometry and the interconnection through pore throats have a greater influence on the flow behaviour. Mercury injection results reported by Xu et al. [29] show that the distribution of pore throat radius is positively correlated with permeability. As shown in Table 1 and Table 4, higher porosity/permeability sample has larger pore size. When the sample has higher permeability, its larger pore size has larger contribution to the permeability.

The grain size of two samples are digitally analysed. The grain size distributions are fairly symmetric distribution (Figure 6) and pore size distributions exhibit tails towards large pore sizes (Figure 5). In the experiments of the varieties of Fontainebleau sandstones, Song et al. observed similar grain size distribution and pore size distribution in the scanning electron microscope (SEM) images and polarized light microscope (transmission) microphotographs of the samples [30]. Table 5 shows the average grain sizes measured are 103.49 and 105.55 µm, respectively, both of which are typical values of sandstone samples. It generally has been recognized by previous studies that grain size is a fundamental independent variable controlling permeability in unconsolidated sediments [30-32]. In the well-known power-law equation, the permeability shows a positive correlation with the square of grain size. Our study shows that grain size becomes smaller under compression to some extent. However, average grain size only changes for about 0.4%. It leads to lower variation on the permeability. Song et al. also observed similar weak stress sensitivity to permeability in most of their Fontainebleau sandstones, especially for low permeability samples [30].

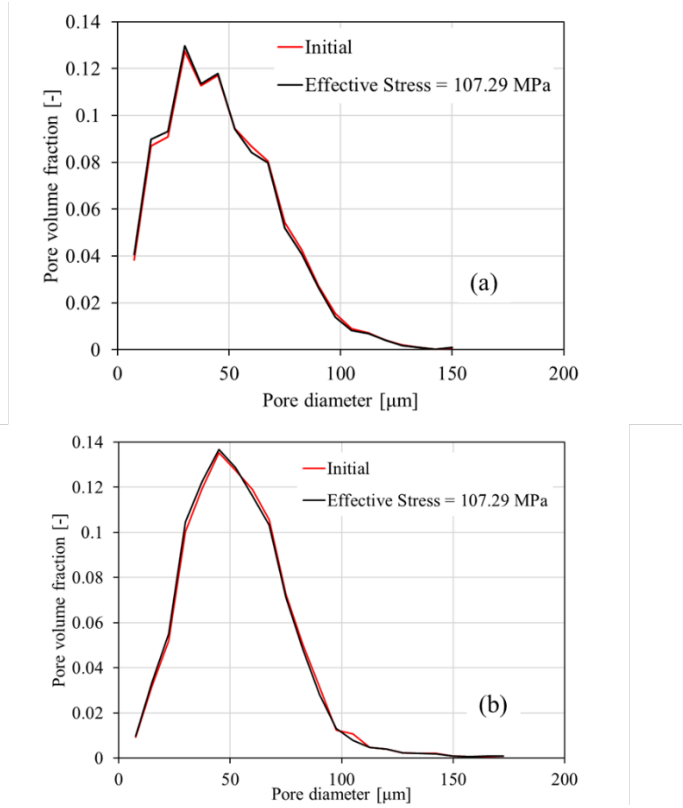

Fig. 5. Distribution of pore diameter for the sample of initial porosity = 12.67% (a) and 23.82% (b) under initial condition (red) and maximum effective stress (black).

Table 4. Average pore diameter at initial and maximum effective stress condition.

Initial porosity [%]	**Initial average pore diameter [µm]**	**Compressed average pore diameter [µm]**	**Difference [%]**
12.67	47.10	46.43	1.42
23.82	53.63	52.95	1.27

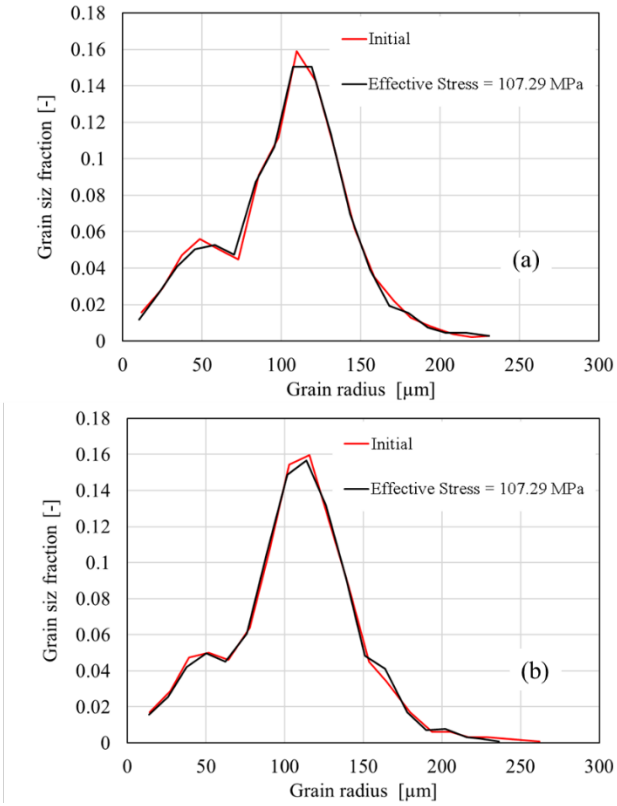

Fig. 6. Distribution of grain radius for the sample of initial porosity = 12.67% (a) and 23.82% (b) under initial condition (red) and maximum effective stress (black).

Table 5. Average grain size at initial and maximum effective stress condition.

Initial porosity [%]	Initial average grain radius [µm]	Compressed average grain radius [µm]	Difference [%]
12.67	103.49	103.09	0.39
23.82	105.55	105.13	0.40

David et al. [4] classified three different mechanisms of compaction. The first type observed in low porosity rock (e.g. crystalline granite) is related to the elastic closure of microfractures, and the sensitivity of permeability to pressure decreases with increasing pressure. The second type observed in a porous clastic rock (e.g. sandstone) has the compaction related to the relative displacement of rock framework grains, and the sensitivity of permeability to pressure is low. The third type has unconsolidated structure (e.g. sand), and there are two different regimes of compaction referred to initial relative displacement of grains (similar to the second type) and grain crushing at elevated pressures. In general, as the sample being compacted, the microfractures are closed initially and then rock framework grains move later, and at last the frame grains are crushed and the pores collapse if elevated pressure is applied beyond critical point. Two samples in this study show the compaction behaviour of the second type and have relative low stress sensitivity of permeability.

The stress dependency of porosity and permeability is mainly due to the change of flow path by deformation under certain stress conditions. The deformation has structural deformation and body deformation. Structural deformation is the pores deformation when the rock framework grains are rearranged. Body deformation is the deformation of rock framework grains. These deformations are observed as shown in Figure 7 and 8.

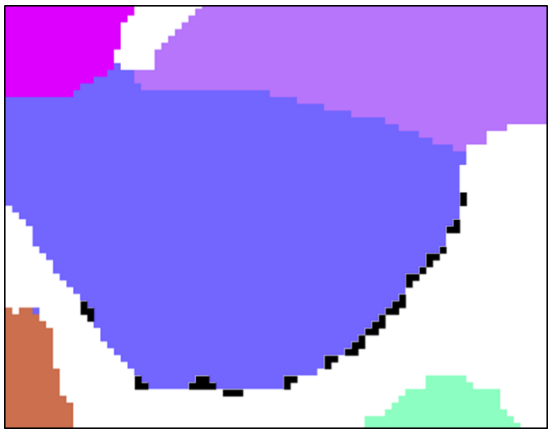

Fig. 7. Body deformation for the sample of initial porosity = 23.82%. Black region indicates porosity change after applying stress.

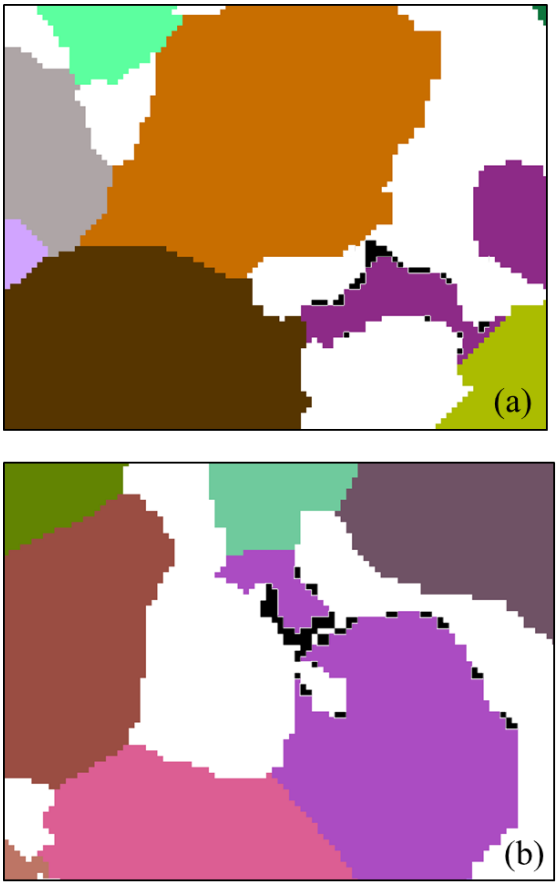

Fig. 8. Structural deformation for the sample of initial porosity = 23.82%: (a) pore shrinking and (b) throat necking. Black region indicates porosity change after applying stress.

3.3 Stress-dependent relative permeability

Next, we present the comparison of multiphase imbibition simulation of water-oil displacement under initial stress condition and maximum effective stress (=107.29 MPa) condition for the sample of low porosity (=12.67%), as shown in Figure 9. In the unsteady-state simulation, oil is continuously displaced by water in the flooding test. A dimensionless parameter, capillary number (Nc), is used to quantify the simulation performed under capillary dominated displacement regime with $N_c \sim 10^{-5}$ [33, 34]. Residual oil saturations were observed to be constant after the injection of 1.0 PV of water for both conditions. Figure 9 shows similar residual oil saturation of 60% for both initial and maximum effective stress conditions. However, effective permeabilities of water and oil phase are lower when the stress is applied. This is because flow paths are constrained due to the deformation of pore structure (Figure 7 and 8).

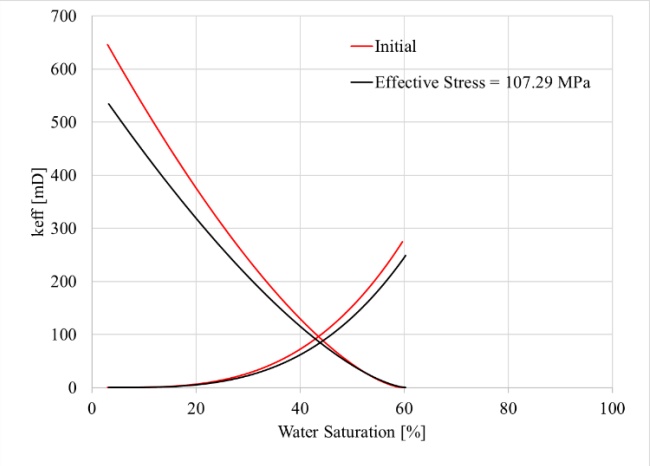

Fig. 9. Effective permeability of water-oil imbibition under initial condition (red) and maximum effective stress (black).

4 Conclusions

We developed a new digital rock workflow coupled with micromechanics to simulate single phase and multiphase fluid flow under realistic subsurface stress condition. In contrast to common fluid simulation at ambient condition, we introduce a micromechanics simulation to predict mechanical response and resulting porosity change under compression condition. In this study, stress dependency of rock porosity and permeability is studied numerically for two sandstone samples. The results showed that, both the porosity and permeability continuously decline with increasing effective stress. The tighter sample shows more stress sensitivity to permeability and porosity. Porosity stress-sensitive behaviour observed in the study is consistent with the reduction behaviour reported in the experimental measurement [4]. However, stress sensitivity to permeability is relatively low due to few microfracture in our sandstone samples. In the multiphase study, the deformation of pore structure after compaction constrains the flow paths of both water and oil phases, and therefore effective permeabilities decrease.

Reference

1. Y. Shi, C.-Y. Wang, 1986. J. Geophys. Res. **91**, 2153–2162 (1986)
2. C.A. Morrow, L.Q. Shi, J.D. Byerlee, J. Geophys. Res.: Solid Earth **89**, 3193–3200 (1984b)
3. J.J. Dong, J.Y. Hsu, W.J. Wu, T. Shimamoto, J.H. Hung, E.C. Yeh, Y.H. Wu, and H. Sone, Int. J. Rock Mech. Min. Sci. **47**, 1141–1157 (2010)
4. C. David, T.-F. Wong, W. Zhu, J. Zhang, Pure Appl. Geophys. PAGEOPH **143**, 425–456. (1994)
5. T. W. Teklu, X. Li, Z. Zhou, H. Abass, SPE Journal, **23**(03), 672-690. (2018)
6. J.W. Schmoker, R.B. Halley, AAPG Bull. **66**, 2561–2570. (1982)
7. J.D. Hoholick, T. Metarko, P.E. Potter, AAPG Bull. **68**, 753–764. (1984)
8. F.O. Jones, W.W. Owens, J. Pet. Technol. **32**, 1631–1640 (1980)
9. J.B. Walsh, Int J Rock Mech Min Sci Geomech Abstr **18**(5): 429–435 (1981)
10. V.V. Petunin, C. Labra, F. Xiao, Fifth Biot Conference on Poromechanics July 10-12, 2013, Vienna, Austria (2013)
11. Z. Sun, H. Tang, D. N. Espinoza, M. T. Balhoff, J.E. Killough, Journal of Petroleum Science and Engineering, **171**, 431-439 (2018)
12. Z. Sun, H. Tang, D. N. Espinoza, M. T. Balhoff, J. E. Killough, SPE Journal, **25**(03), 1543-1556. (2020)
13. S. Fagbemi, P. Tahmasebi, M. Piri, Int. J. Numer. Anal. Methods Geomech. **44**(2), 161–182 (2020)
14. M. Fan, J. McClure, Y. Han, SPE J. **23**(04), 1290–1303 (2018)
15. B. Crouse, D. M. Freed, N. et al. SCA 2016-058 presented at the International Symposium of the Society of Core Analysts held in Snow Mass, Colorado, USA (2016)
16. G.R. Jerauld, J. Fredrich, N. Lane, Q. Sheng, B. Crouse, D. M Freed, R. Xu, In SPE Abu Dhabi International Petroleum Exhibition & Conference. Society of Petroleum Engineers. November (2017)
17. H. Otomo, B. Crouse, M. Dressler, D. M. Freed, I. Staroselsky, R. Zhang, Chen, H, Computers & Fluids, **172**, 674-682 (2018)
18. Fager, H. Otomo, R. Salazar-Tio, G. Balasubramanian, B. Crouse, R. Zhang, H. Chen and J. Schembre-McCabe, The 2021 International Symposium of the Society of Core Analysts (2021): Volume 366
19. Z. Sun, R. Salazar-Tio, A. Fager, B. Crouse, In E3S Web of Conferences (Vol. **366**, p. 01015). EDP Sciences. (2023)
20. Z. Sun, R. Salazar-Tio, L. Duranti, B. Crouse, A. Fager, G. Balasubramanian, Computers and Geotechnics, **135**, 104149. (2021)
21. Abaqus, 2010. Abaqus 6.10 online documentation. Abaqus User Subroutines Ref. Man.

22. X. Shan, H. Chen, Physical Review E, **47**(3), 181 (1993).
23. H. Otomo, H. Fan, Y. Li, M. Dressler, I. Staroselsky, R. Zhang, H. Chen, Journal of Computational Science, **17**, 334-339 (2016)
24. H. Chen, C. Teixeira, K. Molvig, International Journal of Modern Physics C, **9**(08), 1281-1292 (1998)
25. X. Shan, X.F. Yuan, H. Chen, Journal of Fluid Mechanics, **550**, 413-441 (2006)
26. G. Sun, R. Salazar-Tio, J, Yang, H. Otomo, G. Balasubramanian, A. Islam, A. Fager, B. Crouse, R. Zhang, J. Schembre-McCabe, The 2023 International Symposium of the Society of Core Analysts (2023), Vol. **300**
27. H. Andra, N. Combaret, J. Dvorkin, E. Glatt, J. Han, M. Kabel, Y. Keehm, F. Krzikalla, M. Lee, C. Madonna, Comput. Geosci. **50**, 25–32 (2013b)
28. T. Bourbie, B. Zinszner, Journal of Geophysical Research 90 (**B13**), 11524–11532 (1985)
29. C. Xu, C. Lin, Y. Kang, L. You, Rock Mechanics and Rock Engineering, **51**, 2321-2338. (2018)
30. I. Song, & J. Renner, Journal of Geophysical research: solid earth, **113**(B9) (2008)
31. N. R. Morrow, J. D. Huppler, & A. B. Simmons, Journal of Sedimentary Research, **39**(1), 312-321(1969).
32. D. C. Beard, & P. K. Weyl, AAPG bulletin, **57**(2), 349-369 (1973)
33. R. Xu, B. Crouse, D.M. Freed, et al. SCA 2018-066 presented at at the International Symposium of the Society of Core Analysts held in Trondheim, Norway (2018)
34. A. Fager, G. Sun, R. Xu, et al. Journal of Petroleum Science and Engineering, **208**, 109435 (2022)